Article

Preparation of Activated Carbon Doped with Graphene Oxide Porous Materials and Their High Gas Adsorption Performance

Zhiyuan Yang,* Xiaoqian Ju, Hongbin Liao, Zhuoyue Meng, Hailong Ning, Yinyan Li, Zhiping Chen, and Jiang Long

Read Online

ACCESS | Metrics & More | Article Recommendations | Supporting Information

ABSTRACT: It is still a great challenge to develop a new porous carbon adsorbent with excellent separation performance and to recover low-concentration CH_4 in coal mine gas. This work provides a new idea for the study of CH_4 adsorption on activated carbon (AC) composites. Composite materials with microporous structures were prepared from coconut-shell activated carbon (CAC) doped with graphene oxide (GO) by a chemical activation process in this paper. The expansion and dissociation of GO at high temperatures indirectly improve the specific surface area (SSA) of the composite. The interlayer aggregation is reduced, the activation effect is improved, and a new low-cost adsorption material is prepared. The SSA of CAC-50 is more than 3000 $m^2 \cdot g^{-1}$. A high SSA and a narrow pore size distribution lead to a higher total adsorption capacity of CH_4. The breakthrough test also confirmed that AC/GOs had a better adsorption capacity for CH_4. The separation performance of the CH_4/N_2 mixture is not good at room temperature, which is due to the influence of a high SSA and average pore size. As a low-cost and rich material, CAC has a wide range of application prospects. The composite is a potential material for recovering low-concentration CH_4 from the coal mine, which is worthy of attention. In the future, the selectivity of AC/GOs to CH_4 can be increased by loading functional groups or modification.
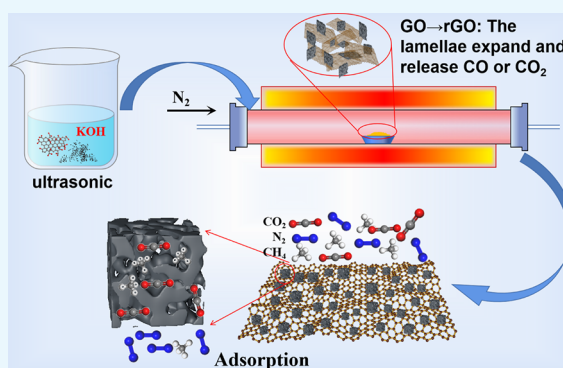
1. INTRODUCTION

Coal mine gas has been liberated during coal mining, about 23 billion to 41 billion cubic meters per year, of which more than 70% is directly vented to the atmosphere.[1] It causes a critical waste of resources while aggravating the greenhouse effect.[2] The analysis of the Global Warming Potential (GWP) shows that in terms of the numbers of molecules, the greenhouse effect of methane is 25 times larger than that of CO_2.[3] In the past three decades, the use of CH_4-based energy has increased significantly, mainly because CH_4 is relatively cleaner and cheaper than petroleum derivatives. Therefore, the enrichment of CH_4 in low-concentration coal mine methane could diminish the greenhouse effect while producing fuel gas concurrently, thereby obtaining significant economic and environmental benefits.

Solvent absorption, low-temperature distillation, and adsorption are commercial technologies for adsorption and separation of coal mine gas.[4,5] The adsorption method has advantages, including mature technology, large capacity, simple operation, and low energy consumption, which is suitable for gas adsorption.[6,7]

Therefore, it is necessary to search for efficient adsorbents applied to the adsorption method. In recent years, various adsorbents were extensively investigated for CH_4 capture,

including metal−organic frameworks (MOFs),[8−10] activated carbon,[11,12] zeolite,[13] and so on. Chang et al.[14] prepared a robust Ca-based metal−organic framework for the separation of CH_4/N_2 for the first time. The MOF had a high CH_4 adsorption capacity (about 20.7 cm^3 (STP)$\cdot g^{-1}$). Yan et al.[15] selected five virtual MOFs from a large number of MOFs, which could potentially adsorb CH_4. These results not only indicated the potential separation targets of CH_4/N_2 but also provided useful information for the large-scale screening of MOFs for other specific separation mixtures. MOFs have high adsorption capacity for CH_4, but there are still some shortcomings, such as high preparation cost, poor chemical stability, and harsh synthesis conditions.[16] Yang et al.[17] successfully prepared nano-ZK-5 by using β-cyclodextrin to control the molecular sieve for the first time. They improved gas adsorption by reducing the size of zeolite crystals. At 298 K, the adsorption capacity of nano-ZK-5 zeolite for CH_4
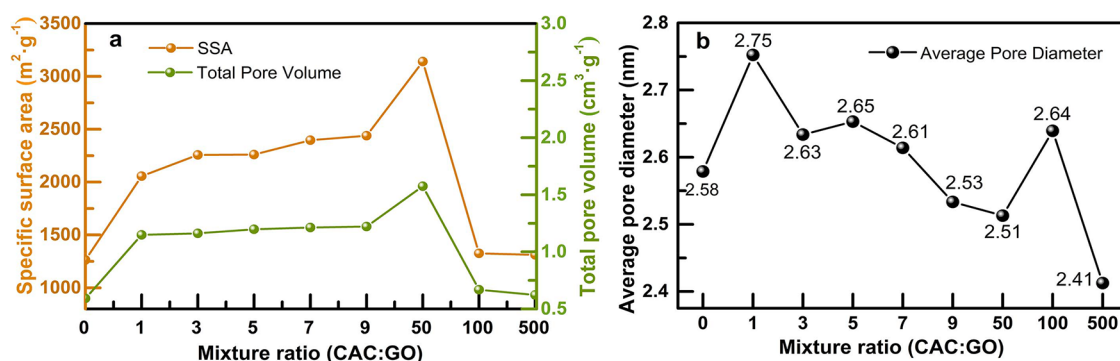
Figure 1. Effects of CAC to GO ratios on SSA (a) and APD of CAC-*X* (b).

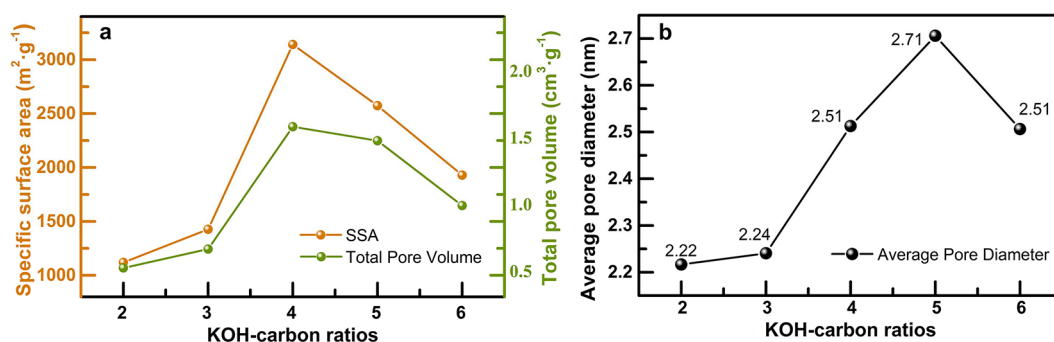**Figure 2.** Effects of alkali to carbon ratios on SSA (a) and APD of CAC50-*Y* (b).

reached a record of 1.34 mmol·g^{-1}. Wu et al.[18] studied the relationship between the crystalline morphology and gas separation performance of L-zeolite. Nano L-type molecular sieves have a higher SSA, total pore volume, and higher gas adsorption capacity. The reason is that the diffusion and mass transfer of nano-L-zeolite are faster due to the shorter channel path. In the process of adsorption, molecular sieves have poor selectivity, low recycling efficiency, and a long synthesis cycle.

Activated carbons (ACs) are recognized in the adsorption field because of their high specific surface area (SSA), well-developed micropores, thermal stability, easy regeneration, and low production cost.[19] Activated carbon from biomass plays a crucial role in the preparation of porous carbon materials. Marco-Lozar et al.[20] used the same measured density in two adsorbents, and the MOF-5 showed a lower volume adsorption capacity and storage capacity than ACs under all gases and conditions studied. Castrillon et al.[21] functionalized commercial activated carbon with NaOH and Fe$_2$CO$_3$ and found that the stronger the alkalinity of NaOH-modified carbon, the more developed the micropores and the higher the selectivity. Ahmed's team[22] had developed a clean way to produce activated carbon from woody biomass. They had reduced chemical use by 70% by using a preheating process. The adsorption capacity of carbon dioxide is 4.22 to 5.44 mmol^{-1}. However, its performance evaluation is too simple (only the CO$_2$ adsorption capacity is tested). Prauchner's team[23] had conducted in-depth studies on different forms of activated carbons for CH$_4$ storage. The adsorbent was prepared by chemical activation of H$_3$PO$_4$ or ZnCl$_2$ and/or physical activation of CO$_2$. It was found that chemical activation can reduce the existence of macropores. Moreover, the bulk density increases by powdering and compressing these samples. The CH$_4$ absorption increases at the same time.

However, the limited specific surface area and micropore volume of AC limit the adsorption capacity. Graphene has a good theoretical SSA, excellent thermochemical stability, and good mechanical properties, which is a potential adsorbent.[24,25] Graphene-based porous adsorbents have application prospects for gas adsorption, capture, and separation.[26,27] In the study of Othman et al.,[28] the dissociation of graphene particles in the thermal treatment process indirectly ameliorated the SSA as well as heightened the adsorption rate of the AC fibers.[29] Based on Lu and Zheng's study,[29] the activation of PAN-based AC nanofibers at the right temperature (800−900 °C) forms a more porous structure with better performance.

By summarizing the literature, we found that a large SSA and pore volume and a narrow pore size distribution (PSD) are the favorable conditions for CH$_4$ absorption. Especially, the pore size is around the optimal particle size for methane adsorption. In this paper, we used ACs as raw materials doped with graphene oxide (GO) to prepare a new type of AC/GO. The doping of the two materials reduces the degree of interlayer aggregation so that the synthesized AC/GOs have more pores. The AC/GOs have an ultra-high SSA and a narrow PSD, which are favorable for methane adsorption. Above all, we prepared an adsorbent with excellent performance and low cost.

2. RESULTS AND DISCUSSION

2.1. Optimization of AC/GO Preparation Conditions. It can be seen from Figure 1 that the addition of GO has a tremendous influence on the pore structure of AC/GO (fixed amount of KOH). As the amount of GO decreased, the SSA of the AC/GO showed an increase followed by a decrease. When the CAC to GO ratio was 50:1, the SSA of CAC-50 was the largest (S_{BET} of 3140.61 m^2·g^{-1}). The average pore diameter (APD) was also relatively small. When the ratio of CAC to GO

was between 1 and 9, the change of the SSA was very slight. When the GO content was the lowest (CAC:GO = 500:1), the SSA value of the CAC-500 was close to that of CAC-0 (activation only, no GO added). In general, the change of the APD with the GO content was evident, and the APD of CAC-50 was the smallest.

The effect of the activator KOH on porosity was studied by fixing the ratio of CAC to GO in Figure 2. The porosities of AC/GOs develop with an increase of the activator. The SSA reaches the maximum when the ratio of alkali to carbon is 4:1. The activation agent continued to increase, and the SSA decreased. A proper amount of the KOH activator can form abundant pores on AC/GO. Yet, an excessive KOH activator will destroy the structure and cause the structure to collapse. This corresponds to the increase in average pore size. Comparison with previous studies is shown in Table S4. The samples in this work have great superiority in adsorption of the pore structure to other studies. More SSA information is shown in Table S5.

The adsorption capacity of methane is positively proportional to the SSA and pore volume of the adsorbent. In the result, we chose CAC-50 with the largest SSA for the following study.

2.2. Performance Characterization.

2.2.1. Surface Functional Groups.
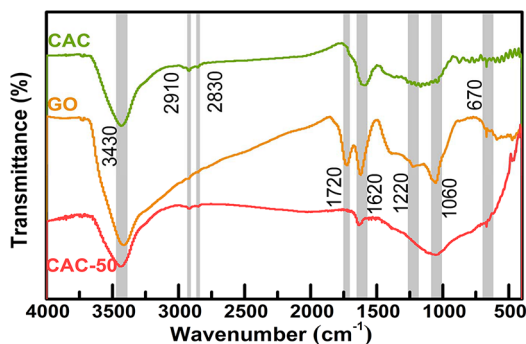Figure 3 shows the infrared spectra of

Figure 3. FTIR spectra of CAC, GO, and CAC-50.

CAC, GO, and CAC-50. The infrared spectra of the raw materials CAC and GO exhibited OH stretching vibration peaks, C=C stretching vibration peaks of the aromatic rings, and the stretching vibration of C−OH at 3430, 1620, and 1060 cm^{-1}, respectively.[30] Moreover, GO exhibited stretching vibration peaks of the carbonyl groups and carboxyl C=O groups at wavenumbers of 1720 and 1220 cm^{-1}, respectively, and a C−O stretching vibration peak of the epoxy group. After composite activation, the vibration peaks of CAC-50 at 1720

and 1220 cm^{-1} disappeared or weakened. This indicated that after the high-temperature pore-forming treatment of the AC/GO, a large number of oxygen-containing functional groups of the material were thermally decomposed and removed. It also indicates that the porous carbon surface retained a small number of oxygen-containing functional groups.

2.2.2. Structural Features.
CAC-0 and CAC-50 were characterized extensively by Raman spectroscopy to infer about the changes in the carbon microstructure. Raman spectra of CAC-0 and CAC-50 obtained are shown in Figure 4a,b. There were two sharp carbon characteristic peaks in the bands of the first order (500−1800 cm^{-1}): a D peak of the turbostratic nongraphitic composition of about 1360 cm^{-1} and a G peak of the representative graphene structure of about 1600 cm^{-1}.[31] Together with these main bands are two amorphous bands A1 (1200 cm^{-1}) and A2 (1550 cm^{-1}), which are usually present in activated carbon. The peak fitting showed that R_{CAC-0} (2.06) > R_{CAC-50} (1.24). The total area of the amorphous region (A1 + A2) changed little. The center of the G peak had also shifted from 1604 to 1598 cm^{-1} moving from CAC-0 to CAC-50. These show that the structure of CAC-50 is more ordered by adding graphene oxide.[32]

In the second-order region, four frequency bands are allocated, such as D″ + D (2480 cm^{-1}), 2D (2700 cm^{-1}), D + G (2930 cm^{-1}), and 2D′ (3150 cm^{-1}). The energy band strength of CAC-50 is higher in the second-order region (1800−3500 cm^{-1}), which proves that the structure of CAC-50 is more ordered.[33] This result indicates that a great quantity of sp^3 C atoms are reduced to sp^2 C atoms during heat treatment.

Figure 5a and Figure 5b show the X-ray diffraction patterns of CAC and CAC-50, respectively. According to Bragg's equation, the distance between the (002) planes (d_{002}), which is the distance between turbine-layered graphite layers, was 0.38 nm for CAC and 0.32 nm for CAC-50. The decrease in the d_{002} value means a total decrease in sp^3 defects, which is consistent with the results of Raman analysis. According to the Scherrer equation,[32] the grain sizes (La) of CAC and CAC-50 were 1.05 and 1.64 nm, respectively, and the stacking heights (Lc) were 0.91 and 0.70 nm, respectively. It is found that the grain size of the samples increases with the addition of GO, but the stacking height decreases. This indicates that the addition of GO makes the sp^2 plane of the sample more ordered, and the existence of CAC avoids the excessive accumulation of GO nanosheets.

2.2.3. Surface Microtopography.
The raw material CAC (Figure 6a) is a block structure with an uneven size, a smooth surface, and no obvious pores. Only KOH-activated samples (Figure 6b,c) show obvious pores on the surface. The pore size is different, and the distribution is not uniform. In the sample
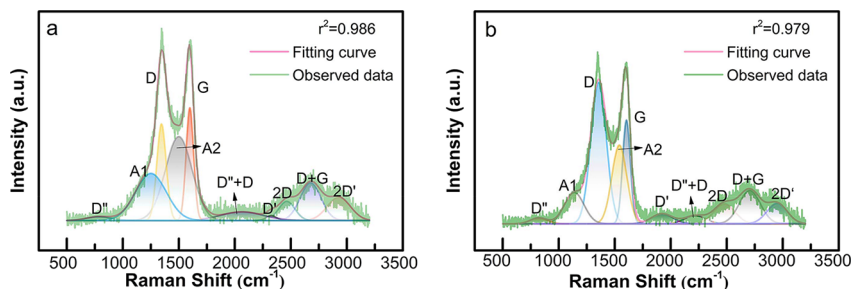

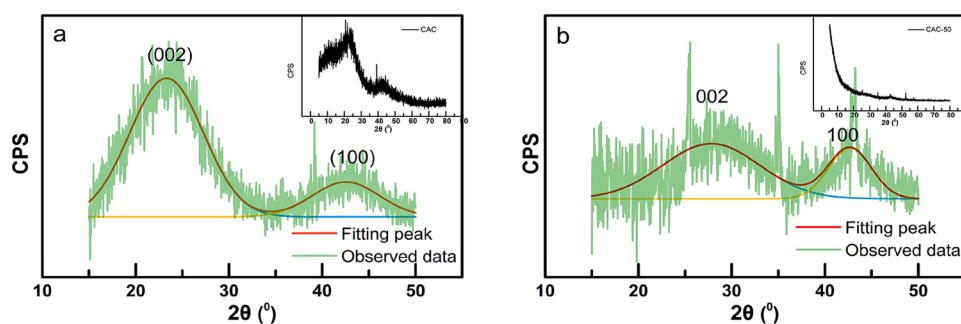**Figure 4.** Raman spectra of CAC-0 (a) and CAC-50 (b).

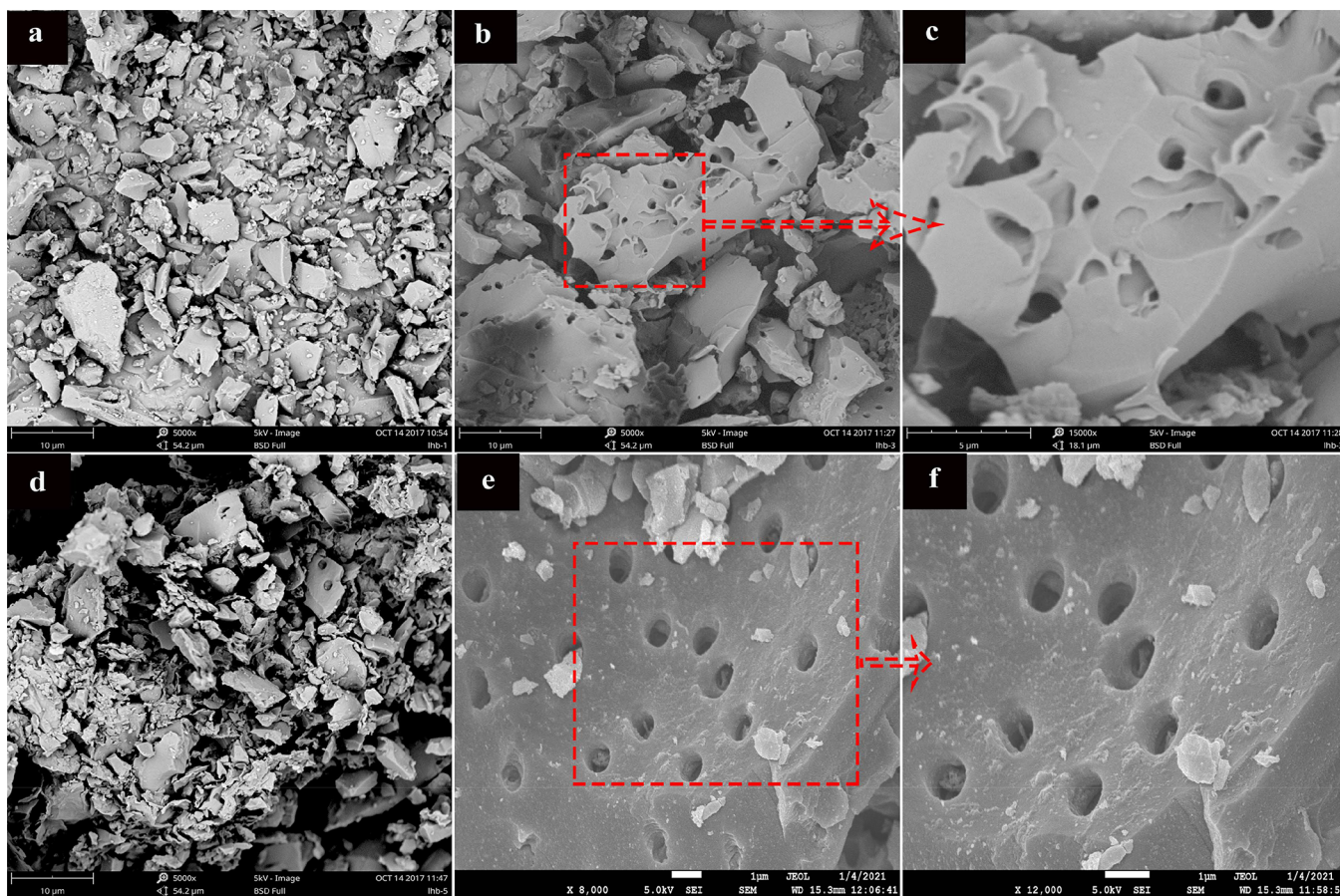**Figure 5.** XRD spectra of CAC (a) and CAC-50 (b).

Figure 6. SEM images of (a) CAC, (b,c) CAC-0, (d) precursor of CAC-50, and (e,f) CAC-50.
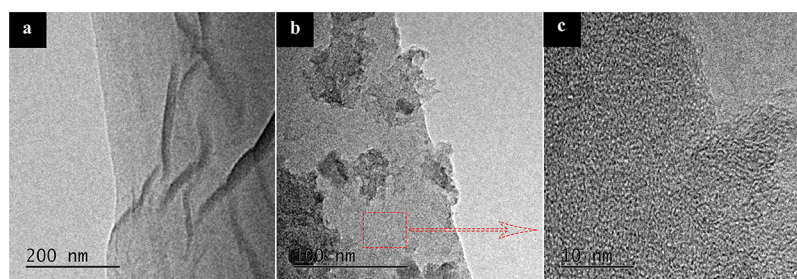

Figure 7. TEM images of (a) GO and (b,c) CAC-7.

only compounded with GO (without KOH activation) (Figure 6D), the particles aggregate. The particles change from the tiled state in Figure 6a to standing on the GO surface. The sample compounded with GO and activated by KOH (Figure 6e,f) has no obvious small particles. Its particle distribution is more uniform.

The size and shape of the pores are more homogeneous. It can also be seen from Figure 7 that after the combination of
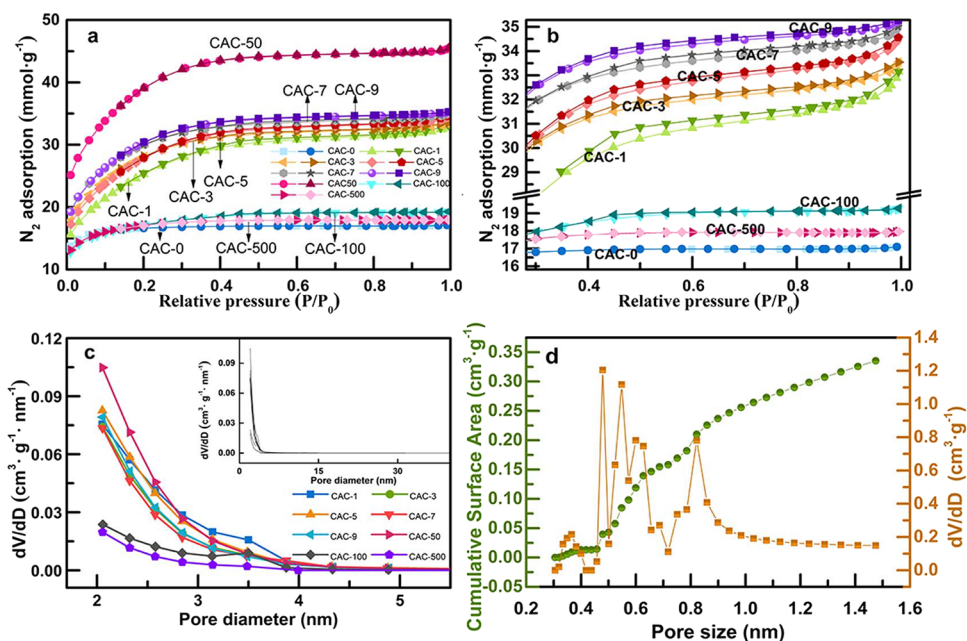
Figure 8. N_2 adsorption−desorption isotherms at 77 K (a), partially enlarged figure (b), pore size distribution (c) of AC/GOs with different proportions of CAC, and pore size distribution of CAC-50 (d).
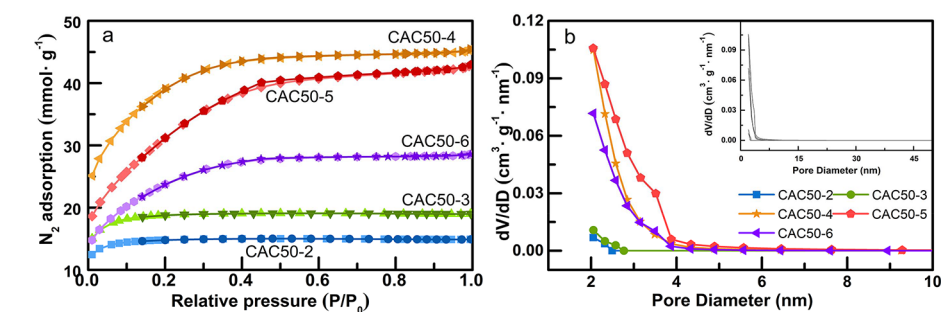

Figure 9. N_2 adsorption−desorption isotherms at 77 K (a) and pore size distribution (b) of CAC-50 with different alkali to carbon ratios.

GO and activated carbon, the surface of the whole sample becomes rough due to the distribution of CAC on the GO surface. The distribution of activated carbon particles was uniform. The results show that CAC is evenly distributed on the GO surface. The AC/GO shows a three-dimensional porous structure.[34]

From the above analysis results, we speculate that in the N_2 atmosphere, the oxygen-containing functional groups on GO lamellae will decompose into CO and CO_2 at a high temperature. The gas increases the pore structure in the material during the overflow process. At this time, the pressure between the lamellae increases rapidly, and the lamellae expand, which makes the material structure looser and the connection of the pore structure more unobstructed.

2.2.4. Pore Structure. The low-temperature nitrogen adsorption test can be used to compare the pore structure changes of AC/GOs under different ratios of CAC to GO (see Figure 8).

With the increase in the GO content, the pore development of AC/GOs increased first and then decreased. The nitrogen adsorption−desorption isotherm of CAC-0 belongs to type I(a). Its isotherm reaches equilibrium at a low relative pressure (about 0.1), which is typical microporous adsorption.[35] With the addition of GO, the adsorption isotherm from CAC-1 to CAC-50 changed to type I(b), and there were weak hysteresis

loops. It shows that the composite has mesoporous structures, and the pore size is very close to the micropore, which is a typical micro-mesoporous structure. It is consistent with the results of the PSD. With the increase in GO, the adsorption isotherms of CAC-100 and CAC-500 changed to type I(a). The results showed that the N_2 adsorption capacity and pore structure of AC/GOs first increased and then decreased with the increase in the GO content. Similarly, an appropriate amount of GO can support CAC. The accumulation of excessive GO leads to the adhesion of the pore structure. The results are consistent with the results of Section 2.3.1. The optimal CAC to GO ratio is 50:1. More pore volume information is shown in Table S5.

The adsorption−desorption curve of CO_2 at 273 K was measured using ASAP2020 equipment of Micrometrics, and the PSD was obtained. Before the test, the sample was degassed at 393 K for 8 h. From Figure 8d, it can be seen that the pore size of the sample is mainly about 0.4−0.8 nm. This is beneficial to the adsorption of CH_4.

In Figure 9, the effects of different alkali carbon ratios on the structure of AC/GOs are compared. The N_2 adsorption capacity of AC/GOs first increases and then decreases with the increase in activator dosage and reaches the maximum when the alkali carbon ratio is 4. The pore size distribution map corresponds to the adsorption curve. When the alkali carbon
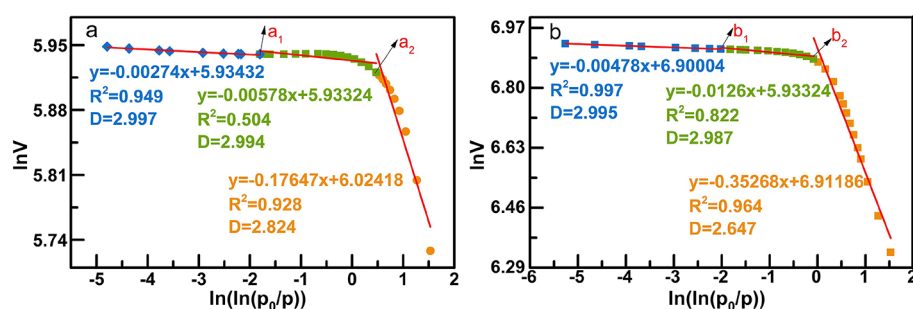
Figure 10. Fractal model fitting diagram of CAC-0 (a) and CAC-50 (b).

ratio is less than 4, the sample pore is microporous, but when the alkali carbon ratio is greater than 4, the sample pore is mesoporous. The main reason is that with the increase in the amount of the activator, the amount of carbon skeleton etching increases, and the effect of pore expansion based on micropores is significant.

2.2.5. Fractal Feature Model of the Pore Structure. The fractal dimension is extensively used to represent the anisotropy and complicacy of the pore structure. The fractal characteristics of pore complexity can be obtained from N_2 (77 K) adsorption data, which mainly shows the fractal character-istics of adsorption pores.[36] The Frenkel−Halsey−Hill model is simple and easy to calculate. Its validity has been confirmed and widely used in the calculation of pore fractal dimensions.[37]

$$\ln V = C + K \ln(\ln(p_0/p)) \tag{1}$$

$$D = 3 + K \tag{2}$$

where V is the adsorption volume of N_2 at equilibrium pressure, $cm^3 \cdot g^{-1}$; C is a constant value; K is a constant; P is the N_2 adsorption equilibrium pressure, MPa; p_0 is saturated vapor pressure of N_2 adsorption, MPa; D is the fractal dimension, which is between 2 and 3. Two cutoff points were selected for each sample. They are the curve inflection points a_1 (b_1) at low pressure (corresponding to adsorption saturation) and the curve rising points a_2 (b_2) at high pressure (corresponding to adsorbate condensation).[38]

Figure 10 shows the fractal fitting diagram. The bigger the D is, the more complex the pore structure is.[39] The D of the two samples is close to 3, indicating that the pores in the samples are rich and complex. In contrast, the D of CAC-50 is smaller than that of CAC-0. Combined with the analysis results of Section 2.2.4, we can see that the addition of GO increases the porosity of the composite samples and makes the pore structure more uniform and orderly. This structure is favorable for the adsorption of CH_4 by CAC-50.

2.3. Adsorption Properties. *2.3.1. Static Adsorption Capacity.* The static adsorption capacities at high pressure (Figure 11) showed that the adsorption capacities of CH_4, CO_2, and N_2 were different for different samples at 303 K and 3 MPa. When the pressure was low, the adsorption capacity increased rapidly. With the increase in pressure, the adsorption isotherm changed gradually, and the adsorption capacity of the gas gradually decreased. Comparing the adsorption of different gases, the adsorption capacities of CAC-50 for gases were in the order of CO_2 > CH_4 > N_2. The CH_4 equilibrium adsorption capacity of CAC-50 was 6.87 mmol·g^{-1}, the CO_2 equilibrium adsorption capacity was 10.38 mmol·g^{-1}, and the N_2 equilibrium adsorption capacity was 3.98 mmol·g^{-1}. The amounts of adsorbed gases of the porous carbon were affected
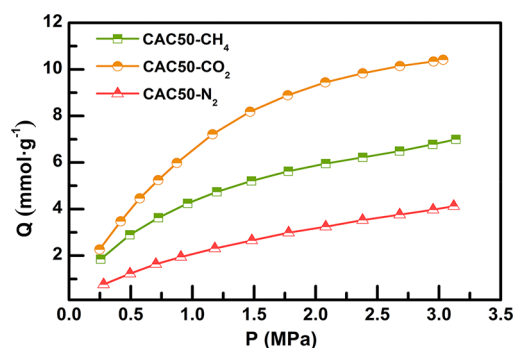

Figure 11. Adsorption isotherms of different gases on CAC-50 at 303 K and pressures up to 3 MPa.

by many factors, and the pore sizes and shapes also had a significant effect. Due to the impact of the PSD, CAC-50 with a large SSA had a low amount of gas adsorption. From Table 1, we can see that the CAC-50 prepared in this paper has certain advantages over the materials reported elsewhere in CH_4 adsorption.

Table 1. Testing Conditions and Methane Adsorption Capacity of Different Biomass Activated Carbons

sample	BET surface area (m²·g⁻¹)	testing conditions	adsorption capacity (mmol·g⁻¹)	reference
CAC-50	3140.67	(303 K, 3 MPa)	6.87	this work
AC-H₃PO₄	1178	(303 K, 3 MPa)	6.52	40
KOH0.5TP50	1372	(298 K, 4 MPa)	5.051	41
activated carbon	1457	(293 K, 3 MPa)	5.382	42
GP32	1407	(298 K, 4.5 MPa)	5.67	43
activated carbon	1290	(303 K, 3 MPa)	3.88	44

2.3.2. Adsorption Model Fitting. By fitting the adsorption isotherm data of different gases on CAC-50 at 303 K and a pressure of 3 MPa (Table S5), the adsorption isotherm models of different adsorbates on CAC-50 are shown in Table 2. The fitting results are shown in Figure 12.

In the Langmuir model equation, q is the adsorption capacity, q_m is the saturated adsorption capacity, b is the adsorption constant reflecting the adsorption strength, and p is the adsorption pressure.[45] In the Freundlich model, n is the model parameter related to the pore distribution and temperature, p is the adsorption pressure, and K is the binding constant. The Langmuir model fitted well, and most of the R^2

Table 2. Fitting Parameters of Different Models

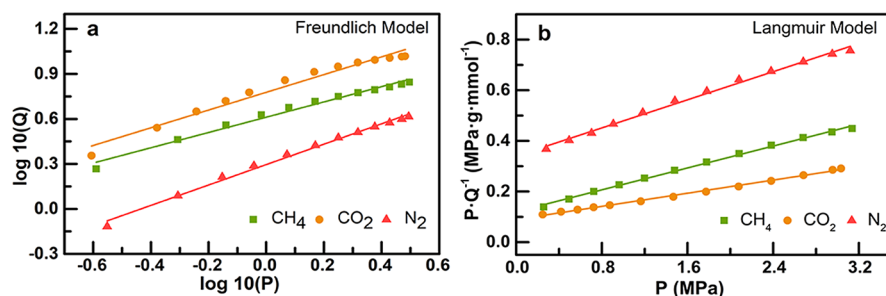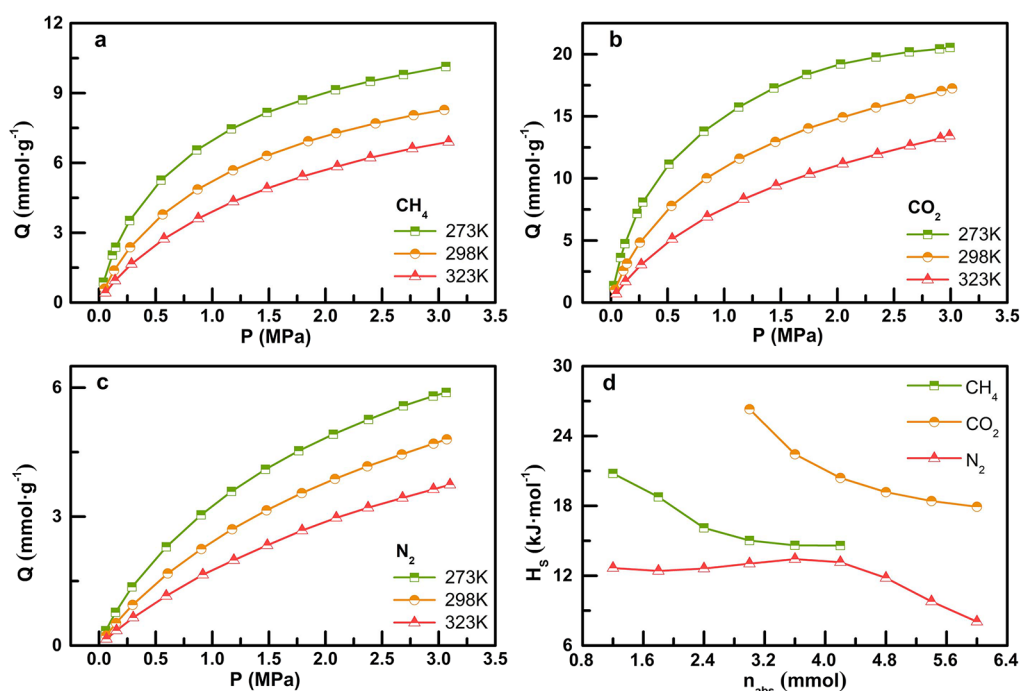| adsorbate	Langmuir model	R^2	q_m (mmol·g^{-1})	b (MPa^{-1})	Freundlich model	R^2	n	K
CAC-50-CH$_4$	$Q = q_m bp/(1 + bp)$	0.997	9.252	0.898	$Q = Kp^{1/n}$	0.983	1.965	4.084
CAC-50-N$_2$		0.994	7.203	0.408		0.993	1.471	1.974
CAC-50-CO$_2$		0.996	15.423	0.723		0.970	1.693	5.984

Figure 12. Freundlich model (a) and Langmuir model (b) fitting for the adsorption of gases on CAC-50.

Figure 13. Adsorption isotherms on CAC-50 of CH$_4$ (a), CO$_2$ (b), and N$_2$ (c) and isosteric heat of adsorption of CH$_4$, N$_2$, and CO$_2$ on CAC-50 (d).

values were above 0.99. Through the calculation of fitting parameters, the saturated adsorption capacity of AC/GO for different gases was determined. The order of saturated adsorption capacity is CO$_2$ > CH$_4$ > N$_2$. The saturated adsorption capacity of CAC-50 for CH$_4$ adsorption is 9.25 mmol·g^{-1}.

2.3.3. Adsorption Thermodynamic Analysis. We selected the sample CAC-50 for the adsorption thermodynamic analysis of different gases. The adsorption isotherms of CH$_4$ at different temperatures on the composite porous carbon (see Figure 13a−c) showed that the equilibrium adsorption decreased with increasing temperature as follows: $Q_{CH_4 - 273 K}$ (10.08 mmol·g^{-1}) > $Q_{CH_4 - 298 K}$ (8.24 mmol·g^{-1}) > $Q_{CH_4 - 323 K}$ (6.82 mmol·g^{-1}), $Q_{CO_2 - 273 K}$ (20.54 mmol·g^{-1}) > $Q_{CO_2 - 298 K}$ (17.18 mmol·g^{-1}) > $Q_{CO_2 - 323 K}$ (13.42 mmol·g^{-1}), $Q_{N_2 - 273 K}$ (5.86

mmol·g^{-1}) > $Q_{N_2 - 298 K}$ (4.74 mmol·g^{-1}) > $Q_{N_2 - 323 K}$ (3.69 mmol·g^{-1}). The high surface temperature was not conducive to the adsorption of the gases on the surface of CAC-50.

Adsorption heat is a significant thermodynamic parameter for studying gas adsorption behavior. It is usually determined based on the adsorption isotherm data of the gas and the Clausius−Clapeyron equation

$$\Delta H_{ST} = -RT^2(\partial \ln p/\partial T)_n \tag{3}$$

where

$$\ln p = -(\Delta H_{ST}/RT) + C \tag{4}$$

The minus sign indicates an exothermic process, ΔH_{ST} is the isosteric heat of adsorption, R is the ideal gas constant, and T is the temperature. We plotted $\ln p$ versus T^{-1} and calculated the isosteric heat of adsorption from the slope of the regression

line.[46] The isoteric heat of adsorption of CH_4, N_2, and CO_2 on CAC-50 is shown in Figure 13d.

The isosteric heats of adsorption of CH_4, CO_2, and N_2 were 20.78−14.59, 26.30−17.93, and 13.43−8.05 kJ·mol^{-1}, respectively. This indicated that the adsorption of the three gases on AC/GO was a physical adsorption process. The isosteric heats of adsorption of the figure showed decreasing trends with increasing adsorption amounts and tended toward fixed values, which indicated that the adsorption position of AC/GO exhibited uneven characteristics. During the adsorption process, the gas was preferentially adsorbed on the stronger surface adsorption sites followed by adsorption at the weaker adsorption sites. Thus, the isosteric heats of adsorption of the gas continuously decreased as the amount of adsorption increased. The adsorption heats of the three different gases on AC/GO indicated that the isosteric heats of adsorption of CO_2 were significantly higher than the adsorption heats of methane and nitrogen, indicating that the preferential order of adsorption of the composite porous carbon was CO_2 > CH_4 > N_2.

2.3.4. Separation Coefficient Calculation. The separation factor is an essential parameter for the selectivity of the reaction adsorbent. Its universal definition for an AB two-component mixture is as follows

$$\alpha_{AB} = \frac{X_A/X_B}{Y_A/Y_B} \tag{5}$$

where X_A/X_B is the molar fraction ratio in the adsorption phase and Y_A/Y_B is the molar fraction ratio in the gas phase.

When the separation factor was used to evaluate the selectivity of the adsorbent to the components of the mixed gas, we calculated the separation factor using the following formula

$$\alpha_{ij} = \frac{q_{m,i}b_j}{q_{m,j}b_j} \tag{6}$$

where $q_{m,i}$ and $q_{m,j}$ are the saturated adsorption quantities of different components in the Langmuir adsorption equation and b_i and b_j correspond to the adsorption strength b in the Langmuir adsorption equation.[47] When the separation coefficient was >2.0, adsorption separation could be achieved theoretically. The larger the separation coefficient, the better the separation effect. We computed the adsorption separation performance at 303 K using the adsorption constant obtained in Section 2.3.2. The high SSA and average pore size result in the loss of selectivity. The adsorption separation factors of different complex materials were calculated, as shown in Figure 14.
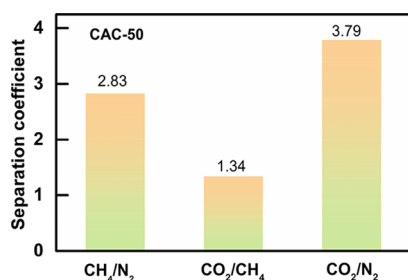

Figure 14. Gas separation performance of CAC-50.

2.3.5. Adsorption Breakthrough Curves. According to the breakthrough curves of different adsorbates, it is determined that methane is first adsorbed at the inlet of the adsorption bed in the dynamic adsorption process. At this time, no detection of CH_4 overflows at the outlet of the adsorption bed. Due to the continuous adsorption of methane, the adsorbent is constantly deactivated, and the mass transfer zone moves steadily to the outlet. At this time, the methane concentration at the outlet increases. Finally, methane saturation in the adsorption bed and the outlet methane concentration are close to the inlet methane concentration.

As can be seen from Figure 15, the breakthrough point of the raw material CAC occurs at 30 s, and 1% concentration
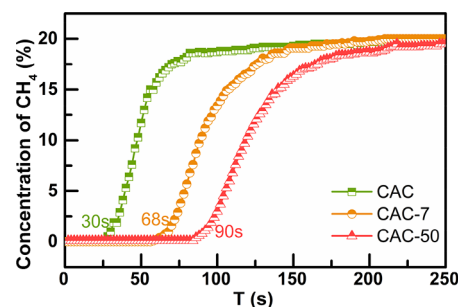

Figure 15. Dynamic adsorption properties of CH_4 on AC/GOs.

(called a breakthrough point) is detected at the outlet. When the binary mixture enters the adsorption bed, the CH_4 concentration at the outlet increases from 0%. The concentration of CH_4 in the outlet reaches 1% at 30 s. At this time, the adsorption bed is penetrated. The CH_4 concentration at the outlet of the adsorption bed increases rapidly, and the adsorbent reaches saturation at a time of 75 s, and the CH_4 concentration at the outlet is stable at the same gas concentration at the inlet. The breakthrough point (1%) of CAC-7 is 68 s, and the adsorption of CAC-50 reaches saturation at 150 s. The breakthrough point of CAC-50 (1%) is 90 s.

Compared with CAC, the CH_4 breakthrough time of CAC-7 was delayed by 38 s and 127%, and that of CAC-50 was delayed by 60 s and 200%. This indicates that adding an appropriate amount of GO will enhance the CH_4 adsorption capacity of AC/GOs. Compared with N_2, CH_4 is a strong adsorption component. So, the AC/GO pressure swing adsorption process can control the separation of CH_4/N_2 in low-concentration coalbed methane. It can realize the enrichment of CH_4 and provide the basis for the beneficiation and resource use of CH_4.

3. CONCLUSIONS

We propose an effective approach of preparing a porous carbon adsorbent with KOH activation using CAC and GO. CAC and GO are selected as sources and then heated at 800 °C and atmospheric pressure under a N_2 atmosphere to prepare AC/GOs, by activation using KOH. Thus, novel AC/GOs with an ultra-high SSA and a narrow micropore size distribution can be obtained.

- The results of the SSA and porosity analysis show that when the mass ratio of CAC to GO is 50:1 and the ratio of alkali to carbon is 4:1, the best AC/GO (CAC-50) is obtained. The SSA of CAC-50 was 3140.61 m^2·g^{-1}.

- The resulting AC/GO exhibited excellent adsorption performance of CH_4. Its CH_4 uptake and CH_4/N_2 adsorption selectivity separately were up to 6.87 mmol·g^{-1} and 2.83 at 3 MPa and 303 K, which were superior to most of the reported powdery carbon materials.

- The morphology and structure characterization results showed that GO increased the pores of AC/GOs and improved the pore connection during pyrolysis. Fractal model fitting shows that the pore structure of CAC-50 is more orderly after adding GO.

- Compared with the breakthrough time of biomass carbon CAC of 30 s, the breakthrough time of CAC-50 was delayed by 200%. The isosteric heat of adsorption of CH_4 was between 14.59 and 20.78 kJ·mol^{-1}. The breakthrough test and adsorption thermodynamics show that AC/GOs are more attractive to CH_4 than N_2. AC/GOs and CH_4 will become potential materials for the industrial/commercial application of CH_4 enrichment in low-level natural gas.

This method is simple and effective, and it is an economic preparation method. It has great potential in the preparation of composite porous carbon materials at a low cost. The carbon adsorbents with a large SSA, uniform pore size, and good separation performance were prepared by this technology, which is worthy of further development.

4. EXPERIMENTAL SECTION

4.1. Materials. The names, specifications, and manufacturers of the reagents involved in the experiment are shown in Table S1. The carbonaceous precursor materials were commercially available graphite powder (Tianjin Kemiou Chemical Reagent Co., Ltd.) and coconut-shell activated carbon (CAC) (Henan Songshan Science and Technology Co., Ltd.). The main properties of CAC were tested following the National Standards of China (GB/T 212-2008 and GB/T 31391-2015), and the results are shown in Table S2.[48]

4.1.1. Preparation of GO. GO was prepared by the Hummers' method.[49] A 1000 mL round-bottom flask was placed in an ice-water bath. Graphite (5 g), 5 g of sodium nitrate ($NaNO_3$), and 150 mL of concentrated sulfuric acid (98%) were added to the flask. After stirring evenly, 15 g of potassium permanganate was added slowly over 30 min in batches. It was stirred for 6 h at 313 K. Next, 200 mL of deionized water was added slowly. At this time, the color of the reaction solution became reddish-brown. After the temperature was raised to approximately 369 K, the solution was stirred fully. The reaction was carried out for 15 min at this temperature. The flask was then removed from the water bath, and 800 mL of deionized water and 40 mL of 30 wt % hydrogen peroxide were added. The color of the solution became bright yellow. After stirring, it was washed seven to eight times with a centrifuge (about 2 h for each washing). After, it was dried in a vacuum-drying oven for 24 h to get GO.

4.1.2. Preparation of AC/GOs. According to the properties of graphene materials, we carried out composite experiments on traditional carbon materials. The GO prepared by the above method was compounded with CAC. The mass ratio of CAC to GO was X:1 (X = 1−500, keeping the amount of CAC unchanged). The ratio of KOH to carbon was fixed to 4:1. The amount of KOH was fixed. The samples were labeled as CAC-X. The mixture was stirred in a 353 K water bath for 2 h. Then, it was sonicated for 2 h. Finally, it was put into a corundum crucible. It was activated in a tube furnace under a N_2 atmosphere. The temperature increased to 1073 K (5 K·min^{-1}), and this temperature was held for 1 h. After, the sample was cooled to room temperature. It was washed using dilute hydrochloric acid and deionized water until the pH was neutral. Then, the AC/GO was obtained. We also examined the effect of the alkali to carbon ratio on the material. The mass ratio of GO to CAC was fixed to 1:50. The tests were conducted based on ratios of alkali to carbon of Y (Y = 6, 5, 4, 3, and 2). The samples were labeled as CAC50-Y. The other steps were the same as above. Details are shown in Table S3. The experimental activation stove is shown in Figure S1.

4.2. Characterization. *4.2.1. Scanning Electron Microscopy (SEM).* The microscopic morphologies of the materials were observed using a Phenom-Pro's benchtop SEM from Phenom-World Company, Netherlands. The magnification was 80−150,000, the resolution was 8 nm, and the acceleration voltage was 5−15 kV.

4.2.2. Transmission Electron Microscopy (TEM). The microstructure of the material was tested using a JEM-3010 high-resolution transmission electron microscope from JEOL. A lanthanum hexaboride electron gun was used, the accelerating voltage was 100−300 kV, the point resolution was 0.14 nm, the lattice resolution was 0.14 nm, and the maximum magnification was 1.5 million times.

4.2.3. Fourier Transform Infrared Spectroscopy (FTIR). The chemical structure analysis of the material was performed using a Thermo Fisher IN10 Fourier transform infrared spectrometer (Thermo Fisher Scientific, USA). The KBr pellet method was used with a resolution of 4 cm^{-1} and a scanning range of 4000−400 cm^{-1}.[50]

4.2.4. Low-Temperature Nitrogen Gas Adsorption−Desorption Test. The SSA and pore structures of the materials were measured using an ASAP2020 physical adsorption instrument (Micromeritics Company). The N_2 adsorption−desorption isotherms of the porous samples at 77 K were determined by the static volumetric method.[51] The SSA values were calculated by the BET method for the adsorption data.[52] The total pore volume data were determined using the adsorbed amounts based on the adsorption isotherm at a relative pressure of 0.99. The PSDs of the porous materials were determined using density functional theory.

4.2.5. X-ray Diffraction (XRD). The crystal structure characteristics of the materials were analyzed using a MiniFlex 600 X-ray diffractometer from Rigaku. The system used a Cu/Kα X-ray source, an operating voltage of 40 kV, an operating current of 200 mA, and a scanning angle range of 2θ = 10−80°.[53]

4.2.6. Raman Spectroscopy. The structural characteristics of the materials were obtained using a LabRAM Aramis Raman spectrometer from HJY, France. The system used an excitation source of 10% and an excitation wavelength of 532 nm.

4.3. Test Methods. *4.3.1. Gas Adsorption Test.* The pure-component gas adsorption capacity test of the CAC-50 adopts a 3H-2000PH2 high-temperature and high-pressure adsorption instrument produced by Bei Shide Instrument Technology (Beijing) Co., Ltd. The static capacity method is used to test the adsorption capacity of materials under different pressures. The repeatability error of the tests was less than ±2%. The samples were predried in a vacuum-drying oven at 378 K for 24 h. During the test, the sample was degassed for 10 h at 378 K and a vacuum of 10^{-4} Pa. The sample tube dead volume and temperature volume were tested using He gas. A vacuum was

applied for 2 h before the adsorption. We waited for the adsorption temperature to be constant. We tested the adsorbed amounts of the pure-component gases (CH_4, CO_2, and N_2) at different partial pressure points.

4.3.2. Breakthrough Test. A schematic diagram of the breakthrough curve test apparatus is shown in Figure 16. The
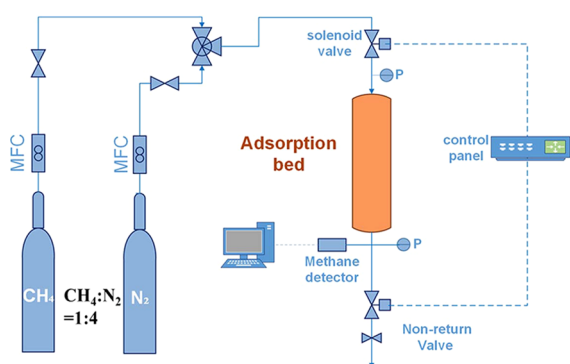

Figure 16. Diagram of CH_4 and N_2 breakthrough curve test process.

AC/GO sample, 2.00 g, was placed in a 600 mm (length) × 22 mm (diameter) chromatographic column. The samples were vacuum-dried at 393 K for 12 h before testing. A vacuum was applied for 1 h before adsorption.[54] The breakthrough experiment was carried out at atmospheric pressure. The flow rate was 120 mL·min^{-1}. The flow ratio of CH_4 to N_2 was 1:4, controlled using two mass flowmeters. The feed gas was mixed in a mixer to achieve the desired concentration. The raw gas was discharged after passing through the AC/GO samples. The concentration of methane was monitored using a methane detector. The breakthrough time was the time corresponding to a CH_4 detection concentration at the outlet of 1%.[55]

ASSOCIATED CONTENT

Supporting Information

The Supporting Information is available free of charge at https://pubs.acs.org/doi/10.1021/acsomega.1c02416.

Picture of the activation stove; names and specification of the reagents; proximate analysis and ultimate analysis of CAC; preparation conditions of AC/GOs; SSA and pore volume information of AC/GOs; adsorption isotherm data of different gases on CAC-50 at 303 K and pressure up to 3 MPa (PDF)

AUTHOR INFORMATION

Corresponding Author

Zhiyuan Yang − *College of Chemistry and Chemical Engineering, Xi'an University of Science and Technology, Xi'an, Shaanxi 710054, China; Key Laboratory of Coal Resources Exploration and Comprehensive Utilization, Ministry of Natural Resources, Xi'an, Shaanxi 710021, China;* orcid.org/0000-0003-1238-3371; Phone: +86-029-85583183; Email: zhiyuanyang@126.com

Authors

Xiaoqian Ju − *College of Chemistry and Chemical Engineering, Xi'an University of Science and Technology, Xi'an, Shaanxi 710054, China*

Hongbin Liao − *College of Chemistry and Chemical Engineering, Xi'an University of Science and Technology, Xi'an, Shaanxi 710054, China*

Zhuoyue Meng − *College of Chemistry and Chemical Engineering, Xi'an University of Science and Technology, Xi'an, Shaanxi 710054, China*

Hailong Ning − *College of Chemistry and Chemical Engineering, Xi'an University of Science and Technology, Xi'an, Shaanxi 710054, China;* orcid.org/0000-0003-2367-5935

Yinyan Li − *College of Chemistry and Chemical Engineering, Xi'an University of Science and Technology, Xi'an, Shaanxi 710054, China*

Zhiping Chen − *College of Chemistry and Chemical Engineering, Xi'an University of Science and Technology, Xi'an, Shaanxi 710054, China*

Jiang Long − *Key Laboratory of Coal Resources Exploration and Comprehensive Utilization, Ministry of Natural Resources, Xi'an, Shaanxi 710021, China*

Complete contact information is available at:
https://pubs.acs.org/10.1021/acsomega.1c02416

Notes

The authors declare no competing financial interest.

REFERENCES

(1) Zhou, F.; Xia, T.; Wang, X.; Zhang, Y.; Sun, Y.; Liu, J. Recent developments in coal mine methane extraction and utilization in China: A review. *J. Nat. Gas Sci. Eng.* **2016**, *31*, 437−458.

(2) Su, S.; Han, J.; Wu, J.; Li, H.; Worrall, R.; Guo, H.; Sun, X.; Liu, W. Fugitive coal mine methane emissions at five mining areas in China. *Atmos. Environ.* **2011**, *45*, 2220−2232.

(3) Zhang, B.; Chen, G. Q. Methane emissions in China 2007. *Renewable Sustainable Energy Rev.* **2014**, *30*, 886−902.

(4) Tahir, M. S.; Shahzad, K.; Shahid, Z.; Sagir, M.; Rehan, M.; Nizami, A. Producing methane enriched biogas using solvent absorption method. *Chem. Eng. Trans.* **2015**, *45*, 1309−1314.

(5) Yousef, A. M.; El-Maghlany, W. M.; Eldrainy, Y. A.; Attia, A. New approach for biogas purification using cryogenic separation and distillation process for CO_2 capture. *Energy* **2018**, *156*, 328−351.

(6) Sircar, S. Pressure swing adsorption. *Ind. Eng. Chem. Res.* **2002**, *41*, 1389−1392.

(7) Möllmer, J.; Lange, M.; Möller, A.; Patzschke, C.; Stein, K.; Lässig, D.; Lincke, J.; Gläser, R.; Krautscheid, H.; Staudt, R. Pure and mixed gas adsorption of CH_4 and N_2 on the metal-organic framework Basolite® A100 and a novel copper-based 1,2,4-triazolyl isophthalate MOF. *J. Mater. Chem.* **2012**, *22*, 10274−10286.

(8) Li, L.; Yang, L.; Wang, J.; Zhang, Z.; Yang, Q.; Yang, Y.; Ren, Q.; Bao, Z. Highly efficient separation of methane from nitrogen on a squarate-based metal-organic framework. *AIChE J.* **2018**, *64*, 3681−3689.

(9) Wu, Y.; Sun, Y.; Xiao, J.; Wang, X.; Li, Z. Glycine-modified HKUST-1 with simultaneously enhanced moisture stability and improved adsorption for light hydrocarbons separation. *ACS Sustainable Chem. Eng.* **2019**, *7*, 1557−1563.

(10) Wang, D.; Xin, Y.; Li, X.; Ning, H.; Wang, Y.; Yao, D. D.; Zheng, Y.; Meng, Z.; Yang, Z.; Pan, Y.; Li, P.; Wang, H.; He, Z.; Fan, W. Transforming Metal-organic frameworks into porous liquids via a

covalent linkage strategy for CO_2 capture. *ACS Appl. Mater. Interfaces* **2021**, *13*, 2600−2609.

(11) Zhao, G.-F.; Bai, P.; Zhu, H.-M.; Yan, R.-X.; Liu, X.-M.; Yan, Z.-F. The modification of activated carbons and the pore structure effect on enrichment of coal-bed methane. *Asia-Pac. J. Chem. Eng.* **2008**, *3*, 284−291.

(12) Zheng, Y.; Li, Q.; Yuan, C.; Tao, Q.; Zhao, Y.; Zhang, G.; Liu, J. Influence of temperature on adsorption selectivity: Coal-based activated carbon for CH_4 enrichment from coal mine methane. *Powder Technol.* **2019**, *347*, 42−49.

(13) Couck, S.; Lefevere, J.; Mullens, S.; Protasova, L.; Meynen, V.; Desmet, G.; Baron, G. V.; Denayer, J. F. M. CO_2, CH_4 and N_2 separation with a 3DFD-printed ZSM-5 monolith. *Chem. Eng. J.* **2017**, *308*, 719−726.

(14) Chang, M.; Ren, J.; Yang, Q.; Liu, D. A robust calcium-based microporous metal-organic framework for efficient CH_4/N_2 separation. *Chem. Eng. J.* **2021**, *408*, 127294.

(15) Yan, T.; Lan, Y.; Liu, D.; Yang, Q.; Zhong, C. Large-scale screening and design of metal-organic frameworks for CH_4/N_2 separation. *Chem. − Asian J.* **2019**, *14*, 3688−3693.

(16) Li, X.; Yang, X.; Xue, H.; Pang, H.; Xu, Q. Metal-organic frameworks as a platform for clean energy applications. *Energy Chem.* **2020**, *2*, 100027.

(17) Yang, J.; Tang, X.; Liu, J.; Wang, J.; Shang, H.; Wu, L.; Li, J.; Deng, S. Down-sizing the crystal size of ZK-5 zeolite for its enhanced CH_4 adsorption and CH_4/N_2 separation performances. *Chem. Eng. J.* **2021**, *406*, 126599.

(18) Wu, L.; Liu, J.; Shang, H.; Li, S.; Yang, J.; Li, L.; Li, J. Capture CO_2 from N_2 and CH_4 by zeolite L with different crystal morphology. *Microporous Mesoporous Mater.* **2021**, *316*, 110956.

(19) Ghanbari, S.; Niu, C. H. Characteristics of oat hull based biosorbent for natural gas dehydration in a PSA process. *J. Nat. Gas Sci. Eng.* **2019**, *61*, 320−332.

(20) Marco-Lozar, J. P.; Juan-Juan, J.; Suárez-García, F.; Cazorla-Amorós, D.; Linares-Solano, A. MOF-5 and activated carbons as adsorbents for gas storage. *Int. J. Hydrogen Energy* **2012**, *37*, 2370−2381.

(21) Castrillon, M. C.; Moura, K. O.; Alves, C. A.; Bastos-Neto, M.; Azevedo, D. C. S.; Hofmann, J.; Möllmer, J.; Einicke, W.-D.; Gläser, R. CO_2 and H_2S removal from CH_4-rich streams by adsorption on activated carbons modified with K_2CO_3, NaOH, or Fe_2O_3. *Energy Fuel* **2016**, *30*, 9596−9604.

(22) Ahmed, M. B.; Hasan Johir, M. A.; Zhou, J. L.; Ngo, H. H.; Nghiem, L. D.; Richardson, C.; Moni, M. A.; Bryant, M. R. Activated carbon preparation from biomass feedstock: Clean production and carbon dioxide adsorption. *J. Cleaner Prod.* **2019**, *225*, 405−413.

(23) Prauchner, M. J.; Sapag, K.; Rodríguez-Reinoso, F. Tailoring biomass-based activated carbon for CH_4 storage by combining chemical activation with H_3PO_4 or $ZnCl_2$ and physical activation with CO_2. *Carbon* **2016**, *110*, 138−147.

(24) Szczęśniak, B.; Choma, J.; Jaroniec, M. Gas adsorption properties of graphene-based materials. *Adv. Colloid Interface Sci.* **2017**, *243*, 46−59.

(25) Alvial-Palavicino, C.; Konrad, K. The rise of graphene expectations: Anticipatory practices in emergent nanotechnologies. *Futures* **2019**, *109*, 192−202.

(26) Wang, D.; Fang, G.; Zheng, Q.; Geng, G.; Ma, J. Construction of hierarchical porous graphene−carbon nanotubes hybrid with high surface area for high performance supercapacitor applications. *J. Solid State Electrochem.* **2017**, *21*, 563−571.

(27) Li, R.; Li, Z.; Wang, G.; Gu, Z. Octadecylamine-functionalized graphene vesicles based voltammetric sensing of hydroquinone. *Sens. Actuators, B* **2018**, *276*, 404−412.

(28) Othman, F. E. C.; Yusof, N.; Ismail, A. F. Activated-carbon nanofibers/graphene nanocomposites and their adsorption performance towards carbon dioxide. *Chem. Eng. Technol.* **2020**, *43*, 2023−2030.

(29) Lu, A.-H.; Zheng, J.-T. Study of microstructure of high-surface-area polyacrylonitrile activated carbon fibers. *J. Colloid Interface Sci.* **2001**, *236*, 369−374.

(30) Meng, Z.; Yang, Z.; Yin, Z.; Li, Y.; Song, X.; Zhao, J.; Wu, W. Effects of coal slime on the slurry ability of a semi-coke water slurry. *Powder Technol.* **2020**, *359*, 261−267.

(31) Ning, H.; Yang, Z.; Wang, D.; Meng, Z.; Li, Y.; Ju, X.; Wang, C. Graphene-based semi-coke porous carbon with N-rich hierarchical sandwich-like structure for efficient separation of CO_2/N_2. *Microporous Mesoporous Mater.* **2021**, *311*, 110700.

(32) Ghosh, A.; Razzino, C. d. A.; Dasgupta, A.; Fujisawa, K.; Vieira, L. H. S.; Subramanian, S.; Costa, R. S.; Lobo, A. O.; Ferreira, O. P.; Robinson, J.; et al. Structural and electrochemical properties of babassu coconut mesocarp-generated activated carbon and few-layer graphene. *Carbon* **2019**, *145*, 175−186.

(33) Brazil, T. R.; Gonçalves, M.; Junior, M. S. O.; Rezende, M. C. A statistical approach to optimize the activated carbon production from Kraft lignin based on conventional and microwave processes. *Microporous Mesoporous Mater.* **2020**, *308*, 110485.

(34) Zheng, C.; Zhou, X.; Cao, H.; Wang, G.; Liu, Z. Synthesis of porous graphene/activated carbon composite with high packing density and large specific surface area for supercapacitor electrode material. *J. Power Sources* **2014**, *258*, 290−296.

(35) Ning, H.; Yang, Z.; Yin, Z.; Wang, D.; Meng, Z.; Wang, C.; Zhang, Y.; Chen, Z. A novel strategy to enhance the performance of CO_2 adsorption separation: Grafting hyper-cross-linked polyimide onto composites of UiO-66-NH_2 and GO. *ACS Appl. Mater. Interfaces* **2021**, *13*, 17781−17790.

(36) Wang, Z.; Cheng, Y.; Zhang, K.; Hao, C.; Wang, L.; Li, W.; Hu, B. Characteristics of microscopic pore structure and fractal dimension of bituminous coal by cyclic gas adsorption/desorption: An experimental study. *Fuel* **2018**, *232*, 495−505.

(37) Avnir, D.; Jaroniec, M. An isotherm equation for adsorption on fractal surfaces of heterogeneous porous materials. *Langmuir* **1989**, *5*, 1431−1433.

(38) Sahouli, B.; Blacher, S.; Brouers, F. Applicability of the fractal FHH equation. *Langmuir* **1997**, *13*, 4391−4394.

(39) Yuan, Y.; Rezaee, R. Fractal analysis of the pore structure for clay bound water and potential gas storage in shales based on NMR and N_2 gas adsorption. *J. Petrol. Sci. Eng.* **2019**, *177*, 756−765.

(40) Peredo-Mancilla, D.; Ghouma, I.; Hort, C.; Matei Ghimbeu, C.; Jeguirim, M.; Bessieres, D. CO_2 and CH_4 adsorption behavior of biomass-based activated carbons. *Energies* **2018**, *11*, 3136.

(41) Arami-Niya, A.; Rufford, T. E.; Zhu, Z. Activated carbon monoliths with hierarchical pore structure from tar pitch and coal powder for the adsorption of CO_2, CH_4 and N_2. *Carbon* **2016**, *103*, 115−124.

(42) Wu, Y.-J.; Yang, Y.; Kong, X.-M.; Li, P.; Yu, J.-G.; Ribeiro, A. M.; Rodrigues, A. E. Adsorption of pure and binary CO_2, CH_4, and N_2 gas components on activated carbon beads. *J. Chem. Eng. Data* **2015**, *60*, 2684−2693.

(43) Vargas, D. P.; Giraldo, L.; Moreno-Piraján, J. C. Carbon dioxide and methane adsorption at high pressure on activated carbon materials. *Adsorption* **2013**, *19*, 1075−1082.

(44) Pino, D.; Bessieres, D. CH_4/CO_2 mixture adsorption on a characterized activated carbon. *J. Chem. Eng. Data* **2017**, *62*, 1475−1480.

(45) Yang, Z.; Ning, H.; Liu, J.; Meng, Z.; Li, Y.; Ju, X.; Chen, Z. Surface modification on semi-coke-based activated carbon for enhanced separation of CH_4/N_2. *Chem. Eng. Res. Des.* **2020**, *161*, 312−321.

(46) Ramirez-Pastor, A. J.; Bulnes, F. Differential heat of adsorption in the presence of an order-disorder phase transition. *Phys. A* **2000**, *283*, 198−203.

(47) Zhou, L.; Zhang, J.; Zhou, Y. A simple isotherm equation for modeling the adsorption equilibria on porous solids over wide temperature ranges. *Langmuir* **2001**, *17*, 5503−5507.

(48) Meng, Z.; Yang, Z.; Yin, Z.; Li, Y.; Ju, X.; Yao, Y.; Long, J. Interaction between dispersant and coal slime added in semi-coke

water slurry: An experimental and DFT study. *Appl. Surf. Sci.* **2021**, *540*, 148327.

(49) He, B.; Shen, Y.; Ren, Z.; Xiao, C.; Jiang, W.; Liu, L.; Yan, S.; Wang, Z.; Yu, Z. Defect-controlled synthesis of graphene based nano-size electronic devices using in situ thermal treatment. *Org. Electron.* **2014**, *15*, 685−691.

(50) Yang, Z.; Yin, Z.; Xue, W.; Meng, Z.; Li, Y.; Long, J.; Wang, J. Construction of Buertai coal macromolecular model and GCMC simulation of methane adsorption in micropores. *ACS Omega* **2021**, *6*, 11173−11182.

(51) Yang, Z.; Li, Y.; Xue, W.; Yin, Z.; Meng, Z.; Zhou, A. Small molecules from multistep extraction of coal and their effects on coal adsorption of CH_4. *Catal. Today* **2021**, *374*, 192−199.

(52) Wang, D.; Xin, Y.; Li, X.; Wang, F.; Wang, Y.; Zhang, W.; Zheng, Y.; Yao, D.; Yang, Z.; Lei, X. A universal approach to turn UiO-66 into type 1 porous liquids via post-synthetic modification with corona-canopy species for CO_2 capture. *Chem. Eng. J.* **2021**, *416*, 127625.

(53) Wang, D.; Xin, Y.; Wang, Y.; Li, X.; Wu, H.; Zhang, W.; Yao, D.; Wang, H.; Zheng, Y.; He, Z.; Yang, Z.; Lei, X. A general way to transform $Ti_3C_2T_x$ MXene into solvent-free fluids for filler phase applications. *Chem. Eng. J.* **2021**, *409*, 128082.

(54) Wang, D.; Ning, H.; Xin, Y.; Wang, Y.; Li, X.; Yao, D.; Zheng, Y.; Pan, Y.; Zhang, H.; He, Z.; Liu, C.; Qin, M.; Wang, Z.; Yang, R.; Li, P.; Yang, Z. Transforming $Ti_3C_2T_x$ MXene into nanoscale ionic materials *via* an electrical interaction strategy. *J. Mater. Chem. A* **2021**, 15441.

(55) Yang, Z.; Wang, D.; Meng, Z.; Li, Y. Adsorption separation of CH_4/N_2 on modified coal-based carbon molecular sieve. *Sep. Purif. Technol.* **2019**, *218*, 130−137.